Neurocomputing 451 (2021) 279–289

Contents lists available at ScienceDirect

Neurocomputing

journal homepage: www.elsevier.com/locate/neucom

Fast and robust multiplane single-molecule localization microscopy using a deep neural network

Toshimitsu Aritake [a,*], Hideitsu Hino [b], Shigeyuki Namiki [c], Daisuke Asanuma [c], Kenzo Hirose [c], Noboru Murata [a]

[a] School of Advanced Science and Engineering, Waseda University, 3-4-1 Okubo, Shinjuku-ku, Tokyo 169-8555, Japan
[b] The Institute of Statistical Mathematics 10-3 Midori-cho, Tachikawa, Tokyo 190-8565, Japan
[c] Graduate School of Medicine, The University of Tokyo, 7-3-1 Hongo, Bunkyo-ku, Tokyo 113-8643, Japan

ARTICLE INFO

Article history:
Received 6 March 2020
Revised 21 August 2020
Accepted 14 April 2021
Available online 20 April 2021
Communicated by Zidong Wang

Keywords:
3D single-molecule localization microscopy
Multi-focal plane microscopy
Lateral drift
Convolutional neural network

ABSTRACT

Single-molecule localization microscopy is a widely used technique in biological research for measuring the nanostructures of samples smaller than the diffraction limit. This study uses multifocal plane microscopy and addresses the three-dimensional (3D) single-molecule localization problem, where lateral and axial locations of molecules are estimated. However, when multifocal plane microscopy is used, the estimation accuracy of 3D localization is easily deteriorated by the small lateral drifts of camera positions. A 3D molecule localization problem was presented along with the lateral drift estimation as a compressed sensing problem. A deep neural network (DNN) was applied to solve this problem accurately and efficiently. The results show that the proposed method is robust to lateral drift and achieves an accuracy of 20 nm laterally and 50 nm axially without an explicit drift correction.

1. Introduction

Fluorescence microscopy is a widely used technique in biological research to analyze in vivo structures of samples. However, owing to the diffraction limit of light, the resolution of conventional fluorescence microscopy is limited to approximately 200 nm laterally and 500 nm axially. To overcome this diffraction limit, several super-resolution microscopy methods [1], including single-molecule localization microscopy (SMLM) [2,3], have been proposed. The fundamental problem in super-resolution microscopy is estimating the true molecular distribution from an observed image. In SMLM, only a few molecules are activated at one time using photoactivatable molecules. Therefore, the positions of the activated molecules can be accurately estimated using a localization algorithm, such as Gaussian fitting. Then, a high-resolution image can be obtained by integrating the localization results from many frames into one image.

In many biological studies, three-dimensional (3D) imaging techniques are important for observing the 3D structures of samples and various 3D fluorescence microscopy techniques have been proposed [4]. In the past decade, SMLM methods have also been extended to achieve 3D super-resolution. The most commonly used method for 3D SMLM is point spread function (PSF) engineering. In particular, several types of filters [5–7] have been proposed to achieve 3D localization. In these methods, the 3D locations of molecules are estimated from the differences in the shape of the PSFs. Hence, additional instruments, such as a cylindrical lenses or phase masks, are required for the optical system, and, the reconfiguration of the optical system for other applications is difficult.

Meanwhile, multifocal plane microscopy (MUM) [8,9], which we used in this work, is a simple extension of two-dimensional (2D) SMLM to 3D using multiple cameras. Fig. 1(a) shows the MUM using four cameras. The 3D locations of the molecules are estimated by the images obtained from multiple focal planes. Additional instruments are not necessary for MUM; thus, the optical layout is simple, and the reconfiguration of the optical system for other applications is relatively easy. However, another problem arises in 3D SMLM using MUM: any lateral drift in the camera positions affects the localization quality. When we use MUM, the camera positions may have sub-pixel-sized lateral drift as shown in Fig. 1(b). Because images from the focal planes are obtained through the same objective lens, the focal planes do not share identical coordinate systems owing to the lateral drifts. The locations of the molecules are estimated from the observations from each focal plane, which is affected by the lateral drift; hence, the drift in the camera positions make the estimation less accurate.

* Corresponding author.
E-mail address: toshimitsu.aritake@ruri.waseda.jp (T. Aritake).

https://doi.org/10.1016/j.neucom.2021.04.050
0925-2312/

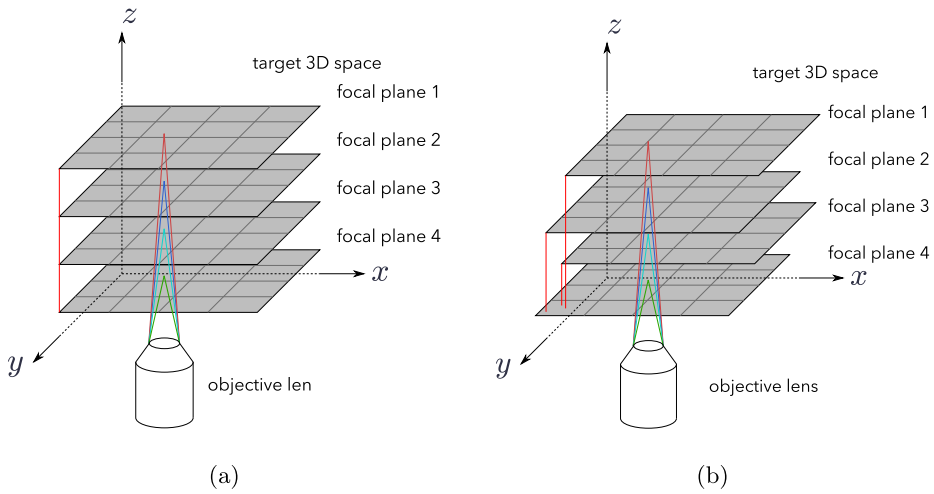

Fig. 1. (a) Ideal multi-focal plane microscopy. Images are simultaneously obtained at each focal plane using an objective lens, and the lateral coordinates of the focal planes are identical. (b) Lateral drift in MUM. Owing to the lateral drift, the lateral coordinates of the focal planes are not identical.

Therefore, for an accurate localization of the molecules, it is essential to compensate for the effect of lateral drift. The MUM proposed in [9] used a cross-correlation approach [10,11] to correct drift between cameras. However, the cross-correlation approach corrects the drift of specimens from a set of localization results at certain time intervals. Then, the molecules must be localized from the observed image obtained from each focal plane independently. Therefore, MUM information is not completely used to localize molecules. Moreover, additional computational cost is required to correct the drift when localizing the molecules.

In this study, we formulated the simultaneous 3D molecule localization and lateral drift correction as a compressed sensing problem [12]. Our formulation uses observed images that are obtained from different focal planes simultaneously and takes advantage of the benefits of MUM for molecule localization and drift correction. By addressing this problem, the locations of molecules are accurately estimated. However, as the size of the input images becomes larger or the target resolution of the localization becomes higher, the problem becomes intractable owing to its high computational cost.

Recently, deep neural networks (DNNs) have been successfully applied to a variety of inverse problems in imaging [13]. Conventionally, inverse problems in imaging were formulated as compressed sensing problems and solved by iterative optimization, which has a high computational cost. Instead of solving the optimization problem iteratively, DNNs use deeply layered networks and approximate the inverse of the observation process by learning the mapping from observations to their corresponding inputs. Intuitively, many iterations of optimization are replaced by a smaller number of trained layers as unrolling methods [14,15].

Recently, DNNs have also been applied to inverse problems of SMLM, such as molecule localization [16–20], colorization [21], and background estimation [22]. Specifically, convolutional neural networks (CNNs) have achieved a remarkable speedup in 2D and 3D molecule localization. Although training a neural network requires a large amount of training data, and the training process can take several hours to several days, the trained network can estimate the molecule locations accurately and efficiently. Moreover, an infinite amount of training data can be generated using an approximated PSF; hence, DNNs are suitable for SMLM.

Here, a CNN was also used to estimate the locations of molecules, along with the lateral drift of cameras instead of solving a compressed sensing problem by an iterative algorithm. We propose a CNN which stacks several deconvolution layers which are used in fast super-resolution convolutional neural network (FSRCNN) [23] for the single image super-resolution of natural images. The architecture of this network is based on the iterative algorithm to solve the compressed sensing problem as unrolling methods. Namely, when we used iterative optimization to solve the compressed sensing problem of molecule localization, the resolution of an input image was enhanced at each iteration. Therefore, the proposed network stacks several deconvolution layers so that the resolution of an input image is enhanced at each layer. As opposed to the super-resolution of natural images, which restores the edges or the textures of an image, the molecule localization only requires to estimate the locations of molecules in an observed image. Therefore, we reformulated the molecule localization problem as a binary classification problem where the network estimates whether a molecule exists in a given pixel of the target resolution. In addition, this network is trained to be robust to lateral drifts in camera positions using the dataset which considers the effect of lateral drifts so that the network can localize molecules accurately without explicit drifts correction. Then, we use the trained network to estimate molecule locations in an observed image.

Our contributions are summarized as follows. First, we formulate the 3D molecule localization problem using MUM as a compressed sensing problem to clarify the inverse problem that we attempt to address in this study. To cope with lateral drift in MUM, the problem aims to estimate the locations of molecules and the amount of lateral drifts of cameras. Then, we point out that the problem becomes intractable owing to the high computational cost when the size of the input images becomes larger or the target resolution of the localization becomes higher. Second, we use CNN to solve the inverse problem approximately, which significantly reduces the computational cost of solving the problem. In addition, this network is trained to be robust to the lateral drift in camera positions. Therefore, the network correctly estimates the molecule distribution from the given input image without explicitly estimating the extent of lateral drift. To the best of the authors' knowledge, this work is the first attempt to tackle the problem of lateral drifts in MUM for SMLM.

The rest of this paper is organized as follows. The observation model and the formulation of the single-molecule localization problem using MUM are explained in Section 2. Then, the problem of the molecule localization using MUM and the details of the

proposed method are presented in Section 3. In the experiments, we used quad-plane microscopy as our MUM method. The detailed experimental setup and experimental results that validate the proposed algorithm are discussed in Section 4. Finally, our concluding remarks and the discussion are provided in Section 5.

2. Formulation

2.1. Observation model

In this study, we used MUM to observe a sample in the target 3D space. The MUM allows the simultaneous imaging at k focal planes in the target 3D space using an objective lens. A conceptual diagram of MUM when $k = 4$ is shown in Fig. 2(a). The intensities of fluorescence are observed as a $W_l \times H_l$ image at each focal plane in the 3D space. Owing to the diffraction limit, low-resolution images are obtained from the focal planes. Hence, we call a set of k observed images as a low-resolution image set.

Let $\boldsymbol{y}^l = (y^l_1, y^l_2, \ldots, y^l_n) \in \mathbb{R}^n$ be a low-resolution image set obtained using MUM, where y^l_i is the observed fluorescence intensity at the i-th observation coordinate $\boldsymbol{x}^l_i = (x^l_{i1}, x^l_{i2}, x^l_{i3}) \in \mathbb{R}^3$, and $n = kW_lH_l$. Note that $\boldsymbol{x}^l_i$ is a coordinate on one of the k focal planes; hence $x_{i3} \in \{d_1, d_2, \ldots, d_k\}$, where d_z $(z = 1, 2, \ldots, k)$ is the depth of the z-th focal plane. The observed image $\boldsymbol{y}^l$ is a convolution of the true molecule density and the PSF which depends on the optical system of a microscope. Therefore, $\boldsymbol{y}^l$ can be approximated by a linear equation as

$$\boldsymbol{y}^l \approx \boldsymbol{H}^*\boldsymbol{c}^*, \tag{1}$$

where $\boldsymbol{H}^* \in \mathbb{R}^{n\times K}$ is an observation matrix. The j-th column of $\boldsymbol{H}^*$ is fluorescence from the j-th molecule, and K is the number of molecules in an image set. The vector $\boldsymbol{c}^* = (c^*_1, c^*_2, \ldots, c^*_K) \in \mathbb{R}^K$ is a molecule distribution, where c^*_j $(j = 1, \ldots, K)$ represents the weight of the intensity of the j-th molecule.

In theory, the true coordinates of molecules can be used to generate $\boldsymbol{H}^*$; however, they are not given or known in advance. Instead, we assumed that the target resolution is given. Hence, we divided a target 3D space into $m = W_h \times H_h \times D_h$ voxels at the target resolution, as shown in Fig. 2 (b). We considered all molecules located at the center of voxels and generated observation matrix $\boldsymbol{H} \in \mathbb{R}^{n\times m}$, instead of $\boldsymbol{H}^*$, where $m \gg K$. We used $\boldsymbol{H}$ and corresponding molecule distribution $\boldsymbol{c} = (c_1, c_2, \ldots, c_m) \in \mathbb{R}^m$ to approximate the observation $\boldsymbol{y}^l$. Here, most of the elements of $\boldsymbol{c}$ are zeros, and weight c_j is nonzero if a molecule is contained in the j-th voxel. We denote the coordinate of the center of the j-th voxel by $\boldsymbol{x}^h_j$ $(j = 1, 2, \ldots m)$.

Then, the (i,j)-element of matrix $\boldsymbol{H}$ is the fluorescence from a molecule at $\boldsymbol{x}^h_j$, observed at $\boldsymbol{x}^l_i$, and can be written as $h(\boldsymbol{x}^l_i, \boldsymbol{x}^h_j)$, where h is a PSF.

$$\boldsymbol{H} = \begin{bmatrix} h(\boldsymbol{x}^l_1, \boldsymbol{x}^h_1) & \cdots & h(\boldsymbol{x}^l_1, \boldsymbol{x}^h_m) \\ h(\boldsymbol{x}^l_2, \boldsymbol{x}^h_1) & \cdots & h(\boldsymbol{x}^l_2, \boldsymbol{x}^h_m) \\ \vdots & \ddots & \vdots \\ h(\boldsymbol{x}^l_n, \boldsymbol{x}^h_1) & \cdots & h(\boldsymbol{x}^l_n, \boldsymbol{x}^h_m) \end{bmatrix} \in \mathbb{R}^{n\times m}$$

We assumed that an observed image contains both shot noise and additive observation noise. The shot noise follows a Poisson distribution, whereas the observation noise follows a Gaussian distribution for each observation independently. Hence, the observation can be modeled as

$$\boldsymbol{y}^l = \boldsymbol{H}\boldsymbol{c} + \boldsymbol{\epsilon}. \tag{2}$$

where $\boldsymbol{\epsilon}$ is composed of shot noise and observation noise.

Now, the problem of molecule localization is to estimate the weights c_j for all $j = 1, 2, \ldots m$ from a low-resolution image set $\boldsymbol{y}^l$. Here, the observation matrix $\boldsymbol{H}$ is an overcomplete matrix $(n < m)$; thus, coefficient vector $\boldsymbol{c}$ cannot be recovered by minimizing the noise in Eq. (2). We assum that $\boldsymbol{c}$ is a sparse vector, where most of the elements are zeros; therefore, $\boldsymbol{c}$ can be recovered by solving the following problem:

$$\underset{\boldsymbol{c}}{\text{minimize}}\ \|\boldsymbol{y}^l - \boldsymbol{H}\boldsymbol{c}\|_2^2 + \lambda\|\boldsymbol{c}\|_1, \tag{3}$$

which is known as Lasso (see [24] and the references therein). This type of inverse problem is known as compressed sensing [12].

2.2. 3D PSF

In the above formulation, the true PSF h is also not known generally; therefore, we used a parametric function, $\hat{h}$, to approximate h, and an approximated observation matrix, $\hat{\boldsymbol{H}}$, to solve Eq. (3). The PSF of MUM is modeled based on the following function:

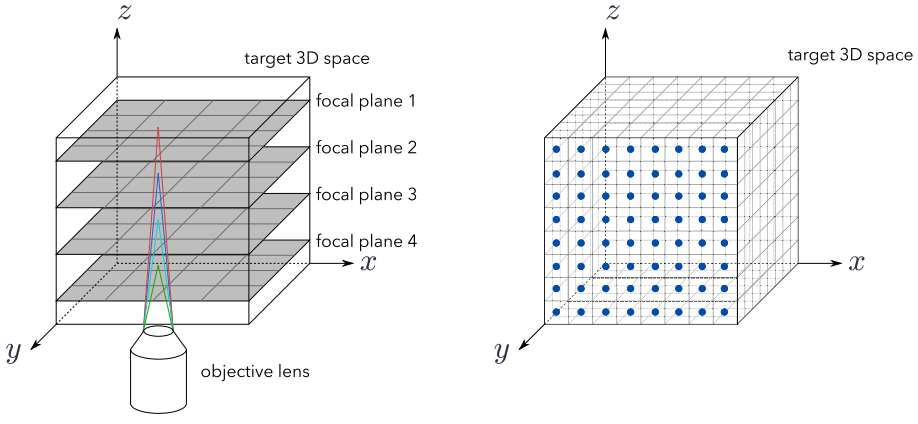

Fig. 2. (a) Illustration of multi-focal plane microscopy observing a sample in 3D space. (b) 3D space divided into voxels at the target resolution. Molecules located at the centers of the voxels are used to approximate an observation. The molecules of the frontmost voxels are shown by the blue circles.

$$\begin{aligned}\hat{h}(\boldsymbol{x}_i^l, \boldsymbol{x}_j^h) &= \hat{h}(x_{i1}^l, x_{i2}^l, x_{i3}^l, x_{j1}^h, x_{j2}^h, x_{j3}^h) \\ &= a(x_{i3}^l - x_{j3}^h) \exp\left(-\frac{(x_{i1}^l - x_{j1}^h)^2 + (x_{i2}^l - x_{j2}^h)^2}{2w(x_{i3}^l - x_{j3}^h)}\right) + b, \end{aligned} \tag{4}$$

where a is the peak fluorescence intensity, w is the squared width of the fluorescence, and b is the background fluorescence intensity. This PSF is similar to the PSF used in [25] for biplane microscopy. The squared width $w(x_3)$ of the PSF varies depending on the distance between a molecule and the focal planes; it is described by the following defocus curve:

$$w(x_3) = w_0^2\left\{1 + \left(\frac{x_3}{d}\right)^2 + A\left(\frac{x_3}{d}\right)^3 + B\left(\frac{x_3}{d}\right)^4\right\},$$

where w_0 is the width of the PSF when a molecule is on the focal plane and d is the focus depth of the microscope. Peak a of the PSF depends on the width $w(x_3)$ and is modeled as:

$$a(x_3) = \frac{a'}{2\pi w(x_3)^2}. \tag{6}$$

The parameters a', b, d, A, and B are determined as listed in Table 1 using a set of images of fluorescent beads obtained from different depths. Namely, these parameters are fitted to a small number of real observations, so that Eq. (4) is close to the real observations. Fig. 3 shows the width of the observed fluorescent beads and the values of the defocus curve (5).

2.3. Lateral drift of the focal planes

When we used MUM to localize the molecules, we must consider the lateral drift of the focal planes. Otherwise, the estimation accuracy of the localization becomes deteriorated because the appropriate observation matrix $\boldsymbol{H}$ varies depending on the drift.

Let Δ_{z1} and $\Delta_{z2} \in \mathbb{Z}$ $(z = 1, 2, \ldots, k)$ be the amount of lateral drift along the horizontal and vertical axes of the z-th focal plane, respectively. In this study, we only considered high-resolution voxel-level lateral drifts. The drift vector is written as $\boldsymbol{\Delta}_z \equiv (\Delta_{z1}, \Delta_{z2}, 0)$. The PSF was defined in Eq. (4), and the following equation holds for $\hat{h}(\boldsymbol{x}_i^l, \boldsymbol{x}_j^h)$:

$$\hat{h}(\boldsymbol{x}_i^l + \boldsymbol{\Delta}_z, \boldsymbol{x}_j^h) = \hat{h}(\boldsymbol{x}_i^l, \boldsymbol{x}_j^h - \boldsymbol{\Delta}_z), \tag{7}$$

where the observation coordinates $\boldsymbol{x}_i^l$ is on the z-th plane. This equation implies that the observation from the molecule at $\boldsymbol{x}_j^h$ with a lateral drift of $\boldsymbol{\Delta}_z$ is identical to the observation from the molecule at $\boldsymbol{x}_j^h - \boldsymbol{\Delta}_z$ without any lateral drift. As the observation from each plane is affected by each drift in camera position, the locations of a molecule estimated from the images obtained from each focal plane are not identical. However, the problem Eq. (3) considers all focal planes to estimate the location of a molecule. Hence, unless we quantify the amount of lateral drift for each plane, the true molecule position cannot be correctly estimated even when a single molecule exists in the 3D space.

Table 1
PSF parameters.

Parameter	Value
a'	5.00×10^7
b	0
w_0	1.33×10^2
d	3.02×10^2
A	7.37×10^{-4}

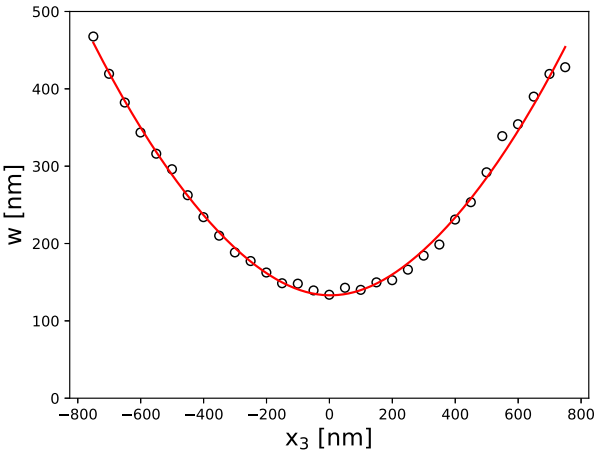

Fig. 3. Width of the observed fluorescent beads and values of the defocus curve. The observed widths of the fluorescent beads at each depth are indicated by circles. The red line shows the value of the defocus curve that approximates the width using the parameters in the Table 1.

Further, based on Eq. (7), if $\boldsymbol{\Delta}_z$ is the same for all $z = 1, 2, \ldots, k$, we cannot distinguish whether the amount of lateral drifts is $\boldsymbol{\Delta}_z$ or true location of the molecule is $\boldsymbol{x}_j^h - \boldsymbol{\Delta}_z$, even when we use the images of all planes. Instead, we estimated the relative lateral drift $\boldsymbol{\Delta}_z' = \boldsymbol{\Delta}_z - \boldsymbol{\Delta}_1$ $(z = 2, \ldots, k)$ from a reference plane $z = 1$. In this study, the amount of relative lateral drift, as well as the molecule positions, were estimated at a high-resolution voxel level.

3. Method

3.1. Compressed sensing with lateral drift estimation

When solving the molecule localization problem stated in Eq. (3), the lateral drift of the focal planes should be considered to estimate the molecule location accurately. The approximated observation matrix $\hat{\boldsymbol{H}}$ varies depending on the lateral drift; hence, the approximated observation matrix $\hat{\boldsymbol{H}}$ can be modified so that the molecule location is correctly estimated.

By ordering the rows of the observation matrix $\hat{\boldsymbol{H}}$ based on the axial position x_{i3}^l of the observation coordinate $\boldsymbol{x}_i^l$ $(i = 1, 2, \ldots n)$, $\hat{\boldsymbol{H}}$ becomes a block matrix

$$\hat{\boldsymbol{H}} = \begin{bmatrix} \hat{\boldsymbol{H}}_1 \\ \hat{\boldsymbol{H}}_2 \\ \vdots \\ \hat{\boldsymbol{H}}_k \end{bmatrix}, \tag{8}$$

where each submatrix $\hat{\boldsymbol{H}}_z \in \mathbb{R}^{n' \times m}$ represents the observation matrix of the z-th focal plane and $n' = \frac{n}{k}$. As the lateral drift affects each plane independently, the drift of each block can be considered individually. Submatrices shifted by $\boldsymbol{\Delta}_z'$ $(z = 2, \ldots, k)$ are written as follows:

$$\hat{\boldsymbol{H}}_z(\boldsymbol{\Delta}_z') \equiv \begin{bmatrix} \hat{h}(\boldsymbol{x}_1^l - \boldsymbol{\Delta}_z', \boldsymbol{x}_1^h) & \cdots & \hat{h}(\boldsymbol{x}_1^l - \boldsymbol{\Delta}_z', \boldsymbol{x}_m^h) \\ \hat{h}(\boldsymbol{x}_2^l - \boldsymbol{\Delta}_z', \boldsymbol{x}_1^h) & \cdots & \hat{h}(\boldsymbol{x}_2^l - \boldsymbol{\Delta}_z', \boldsymbol{x}_m^h) \\ \vdots & \ddots & \vdots \\ \hat{h}(\boldsymbol{x}_{n'}^l - \boldsymbol{\Delta}_z', \boldsymbol{x}_1^h) & \cdots & \hat{h}(\boldsymbol{x}_{n'}^l - \boldsymbol{\Delta}_z', \boldsymbol{x}_m^h) \end{bmatrix}.$$

Here, we consider the maximum amount of shift is given as a hyperparameter.

Now, the problem is to estimate both the lateral drifts and the molecule locations from the observation $\boldsymbol{y}^l$, which can be formulated as:

$$\underset{\{\boldsymbol{c}_t\}_{t=1}^T,\{\Delta_z'\}_{z=2}^k}{\text{minimize}} \sum_{t=1}^{T}\left(\|\boldsymbol{y}_t^l - \hat{\boldsymbol{H}}(\{\Delta_z'\}_{z=2}^k)\boldsymbol{c}_t\|_F^2 + \lambda\|\boldsymbol{c}_t\|_1\right), \tag{9}$$

where

$$\hat{\boldsymbol{H}}(\{\Delta_z'\}_{z=2}^k) = \begin{bmatrix} \hat{\boldsymbol{H}}_1 \\ \hat{\boldsymbol{H}}_2(\Delta_2') \\ \vdots \\ \hat{\boldsymbol{H}}_k(\Delta_k') \end{bmatrix}. \tag{10}$$

Here, we considered T images simultaneously to ensure that the amount of lateral drifts is correctly estimated from the images. As we assumed that only a small number of molecules exist in the target 3D space, estimating all the lateral drifts from a single image is not always possible.

However, the optimization problem above has a high computational cost because we need to consider all the possible pairs of lateral drifts to obtain an optimal solution. Although this problem can be solved by alternating the optimization of $\{\boldsymbol{c}\}_{t=1}^T$ and $\{\Delta_z'\}_{z=2}^k$ to obtain a sub-optimal solution, the optimization of $\{\boldsymbol{c}_t\}_{t=1}^T$ has an increasingly high computational cost as the input image size becomes larger or the target resolution of the molecule localization becomes higher. Moreover, the optimization with respect to $\{\boldsymbol{c}_t\}_{t=1}^T$ is solved using an iterative algorithm. The slow computational speed prevents us from applying 3D SMLM using MUM for interactive observation. Therefore, a faster method for solving the optimization problem is required to obtain a super-resolution image within a reasonable computational time.

3.2. Convolutional neural network (CNN)

In this study, we used a CNN to reduce the computational cost to solve the optimization problem Eq. (9). We assumed that the resolution of the input and output images is given, and the scaling factor is $8\times$ along each axis and the number of focal planes is $k = 4$ henceforth. As the other SMLM methods using DNNs [16–20], the CNN was used to reduce the computational cost of the optimization with respect to $\boldsymbol{c}_t$.

We propose a CNN which is composed of several convolution layers and deconvolution layers, as shown in Fig. 4. The main building blocks of the network are the deconvolution layers, which are used in FSRCNN [23] for single image super-resolution of natural images. Unlike FSRCNN, which uses only one deconvolution layer at the last layer, the first convolution layer extracts features from an input image, followed by the three deconvolution layers. As we assume that the scaling factor is $8\times$, based on the doubling the lateral resolution of an input image at each layer, we used three deconvolution layers. For these layers, we also used a rectified linear unit, also known as ReLU, as our activation function, followed by batch normalization layers [26], to enhance the training speed and the estimation accuracy for these layers. For the last layer of the network, a convolution layer followed by a sigmoid function is used to obtain a set of images for the target axial resolution. Unlike a natural image super-resolution task, the localization problem in Eq. (3) aims to estimate the existence of a molecule in each high-resolution voxel. Hence, the network outputs the probability of the existence of a molecule in each voxel using a sigmoid function as an activation function. In other words, at the last layer of the network, the binary classification problem, where the network estimates whether a molecule exists or not, is solved for each voxel.

The architecture of the proposed network is based on iterative optimization to solve the compressed sensing problem Eq. (9), and the proposed network can be seen as one of the unrolling methods [14,15]. When we used iterative optimization to solve the compressed sensing problem, as in Eq. (9), each iteration enhances the resolution of the estimated output. Namely, a deconvolution problem is solved and an input image is upsampled and deblurred at each iteration. Therefore, to mimic the iterative deconvolution process, we stacked deconvolution layers so that the resolution of a low-resolution input image is doubled at each deconvolution layer while features for the localization are extracted. Intuitively, many iterations of optimization algorithm are replaced by a smaller number of trained layers as unrolling methods.

The input of the network is the observed low-resolution image that is possibly affected by the drift in camera positions, and the output is the estimated molecule distribution. The network was trained to minimize the error between the true molecule distribution and the distribution which is estimated from the observed image. In addition, the network was trained to be robust to the lateral drifts in camera positions so that the trained network can correctly estimate the molecule distribution without explicitly estimating the amount of lateral drifts $\{\Delta_z'\}_{z=2}^k$. To train the robust network, artificial data which are affected by the random lateral drifts are used and parameters of the network are optimized to localize molecules from images that are affected by the lateral drifts.

Let $\boldsymbol{p} = (p_1, p_2, \ldots p_m)$ be the ground-truth molecule existence probability for each voxel, where

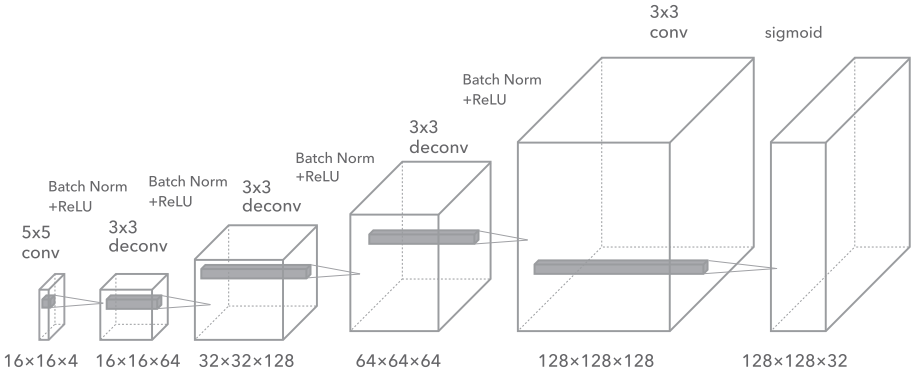

Fig. 4. Network architecture of the proposed model.

$$p_j = \begin{cases} 0 & c_j = 0, \\ 1 & c_j > 0, \end{cases} \tag{11}$$

and let $\boldsymbol{q} = (q_1, q_2, \ldots, q_m)$ be the probability of the existence of a molecule as estimated by the CNN. As the network solves the binary classification problem at each voxel, we used the sum of the binary cross-entropy (BCE):

$$\ell(\boldsymbol{p}, \boldsymbol{q}) = \sum_{j=1}^{m} \left(-p_j \log(q_j) - (1 - p_j) \log(1 - q_j)\right),$$

as the loss function to train the network.

To train the network, we need a training dataset. However, the true molecule density of the real samples is not known. Therefore, we used artificial low-resolution images generated from artificial distributions to train the network.

We generated random molecule distributions that contain K molecules in a 3D space. In this study, $K = 3$ was used; the size of the target 3D space is 3072 nm $\times$ 3072 nm $\times$ 1600 nm, and the coordinates of the molecules $\boldsymbol{x}_j^*$ $(j = 1, 2, \ldots, K)$ were independently drawn from a uniform distribution on this space. The weight c_k^* $(j = 1, 2, \ldots, K)$ of each molecule was also independently drawn from a continuous uniform distribution on $[0.3, 1.0]$, and the target value $\boldsymbol{p}$ was generated as in Eq. (11).

We assumed that the size of the low-resolution image obtained from each focal plane is 16 $\times$ 16 and the size of each pixel of images is 192 nm $\times$ 192 nm. The size of the high-resolution voxel is 24 nm $\times$ 24 nm $\times$ 50 nm, and a high-resolution image set is composed of 32 images of size 128 $\times$ 128. The relative lateral drift of the focal planes $\Delta'_{z1}, \Delta'_{z2}$ $(z = 2, \ldots, 4)$ are randomly chosen as $24s$ nm independently, where s is drawn from a discrete uniform distribution on $[-2, 2] \subset \mathbb{Z}$. Then, low-resolution images are generated by calculating the values of $\sum_{k=1}^{K} \hat{h}(\boldsymbol{x}, \boldsymbol{x}_k^h)$ on the low-resolution grids $\boldsymbol{x} = \boldsymbol{x}_i^l$ $(i = 1, 2, \ldots, n)$.

To generate a training dataset, the coordinates of the molecules $\{\boldsymbol{x}_j^*\}_{j=1}^{K}$ and the relative lateral drifts of the focal planes $\{\Delta'_{z1}\}_{z=2}^{4}, \{\Delta'_{z2}\}_{z=2}^{4}$ were randomly drawn, as above, for each frame $t = 1, 2, \ldots, T$ independently. By training the network with this dataset, it is expected that the trained network becomes robust to the lateral drifts in camera positions within $[-2, 2]$ high-resolution voxels.

4. Experiments

We showed the experimental results of the localization by our proposed method using both artificial images and the real microscopy images. In the following experiments, images observed by the above microscope were processed on an Nvidia Tesla V100 32 GB GPU to localize molecules in the images.

4.1. Optical layout of the microscope

In this section, the experimental settings of the quad-plane microscope used in the experiments were presented. A multi-focus microscope equipped with four EM-CCD cameras (iXon 897, Andor) was constructed based on a commercial inverted microscope (ECLIPSE Ti, Nikon) (Fig. 5). A 640 nm laser beam (HL6366DG, Thorlabs) that passed through a cleanup filter (LD01-640/8, Semrock) was focused on the back focal plane of a 100$\times$ oil immersion objective (Plan Apo VC 100X/1.40, Nikon) to illuminate an Alexa Fluor 647-stained specimen at an excitation intensity of approximately 5 kW/cm^2. The fluorescence emitted from the specimen was collected by the same objective. A filter cube consisting of an excitation filter (608–648 nm, FF02-628/40, Semrock), a dichroic mirror (669 nm, FF660-Di02, Semrock), and

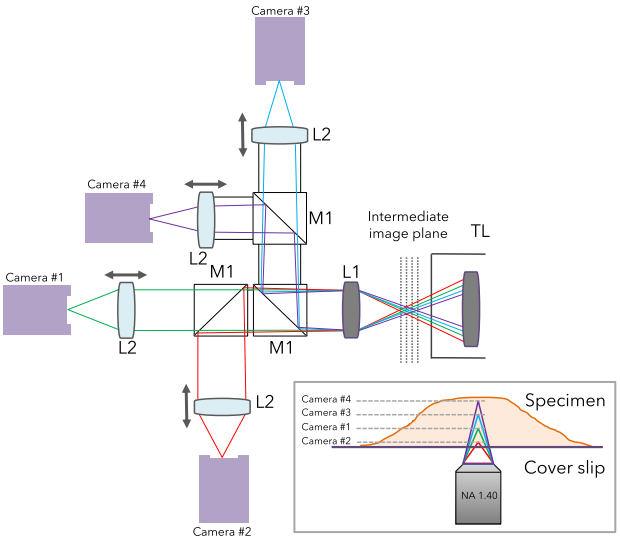

Fig. 5. Optical layout of the quad-plane microscope. The intermediate image is relayed onto each camera via a pair of lenses (L1, f = 125.0 mm; L2, f = 100.0 mm). TL, tube lens; M1, 1:1 beam-splitter mirror. The inset shows the focusing planes of four cameras.

a bandpass mirror (672–712 nm, FF01-692/40, Semrock) was used to separate the excitation and emission light. The fluorescence image formed by the internal tube lens of the inverted microscope was relayed by an achromatic lens (f = 125.0 mm, Thorlabs), split twice by 1:1 beam-splitter mirrors (BSW29R, Thorlabs), and refocused onto the four cameras via achromatic lenses (f = 100.0 mm, Thorlabs). The axial positions of the achromatic lenses in front of the cameras were adjusted so that the four planes at 400 nm intervals in the Z-axis direction of the specimen corresponding to the conjugate planes of the sensor surface of the respective camera. The relative distance among planes was estimated based on a shift in Z-axis position dependence of PSFs, which were determined by imaging fluorescent beads (FluoSphere Carboxylate-Modified Microspheres, 0.2 μm, Invitrogen) while varying Z-axis positions of the objective using a piezo positioner (P725.1, PI). The difference in the field of view of the cameras was corrected by coordinate registration using affine transformation, the parameters of which were determined by images of multiple fluorescent beads captured using different cameras.

Methanol-fixed COS7 cells were used for STORM imaging of tubulin molecules expressing inside the cells as described previously [27]. The primary and secondary antibodies were an anti-tubulin antibody (YL1/2, Abcam) and an Alexa Fluor 647-labeled anti-rat IgG antibody, respectively. The specimen was mounted in a STORM buffer (10 mM NaCl, 60% sucrose, 10% glucose, 0.1% β-mercaptoethanol, 0.5 mg/mL glucose oxidase, 0.04 mg/mL catalase, and 50 mM HEPES, pH 8.0) and then subjected to imaging. Images were acquired at 22 Hz with 20 ms exposure.

4.2. Experiments with artificial images

First, we used two different datasets to assess the effects of lateral drifts for molecule localization. One dataset was affected by the random lateral drifts $\Delta'_k = (\Delta'_{k1}, \Delta'_{k2}, 0)$ $(k = 2, 3, 4)$ for each image independently, and the other dataset did not consider the lateral drifts when generating the artificial images. Then, we used each dataset to train the network. Each dataset consists of 90,000 low-resolution images $\{\boldsymbol{y}_t^l\}_{t=1}^{90000}$ and the corresponding molecule existence probabilities $\{\boldsymbol{p}_t\}_{t=1}^{90000}$ generated from the random mole-

cule distribution. The parameters of the experiments are presented in Table 2. An example of training data is shown in Fig. 6. We used Adam [28] as an optimizer, with the parameters $\beta_1 = 0.9, \beta_2 = 0.99$ and the initial learning rate was set to 1.0×10^{-3}, and the batch size was 100. The dataset was randomly shuffled at the end of each one of 30 epochs.

To assess the effect of lateral drifts, we evaluated the estimation accuracy of the two trained networks. We generated 500 artificial images that contain only one molecule in the 3D space, and the other parameters were the same as the parameters in Table 2. In this experiment, we assumed that a molecule exists in a voxel where the network outputs the highest molecule existence probability. Fig. 7 shows a 2D histogram of the estimation error along x and y axes by two networks. The error is discretized at the resolution of the high-resolution voxels, and the element at (0, 0) shows the number of correctly localized molecules. Further, the Jaccard indices of the classification of the voxels that contain a molecule are shown in the caption. As we can see from the figure, the network that is trained to be robust to the lateral drifts localizes most of the molecules correctly. Meanwhile, the error of the network that is not robust to the lateral drifts distributed to a broader area, and the number of the correctly localized molecules is less than in Fig. 7(a). This result suggests that if we do not consider the effect of the lateral drifts, the accuracy deteriorates even when only one molecule exists in the target space.

We also evaluated the computational speed and localization accuracy of the compressed sensing method and robustly trained network using 500 artificial images that contain only one molecule in the target 3D space. As the previous experiment, the generated images were affected by the lateral drifts. Also, we assumed that the number of molecules in the target space is known for the compressed sensing method. Table 3 shows the average lateral and axial error between the estimated voxel and the true voxel. The lateral error of the CNN is smaller than the lateral error of the compressed sensing. On the other hand, the axial error of the compressed sensing method is smaller than the axial error of CNN, however, this is due to the assumption that the number of molecules is known in advance. Most importantly, when estimating the molecule distribution, CNN process shows much higher fps than the compressed sensing method.

Next, we validated the accuracy of the robustly trained network against lateral drifts. As the previous experiment, we generated artificial images that contain only one molecule in the 3D space and estimated that a molecule exists in the voxel where the network outputs the highest molecule-existence probability. In Fig. 8, the mean localization accuracy along the horizontal (X), vertical (Y), and axial (Z) directions with 95% confidence intervals are shown for each true molecule depth. The figure indicates that the error along each axis is within a high-resolution voxel on average along each axis at all depths.

Fig. 9 shows the estimation results with multiple molecules. The molecules are sampled from the helix curve (red line), and their high-resolution coordinates are shown by red circles. In this experiment, we estimated that the molecules exist in the voxels

Table 2
Parameters for experiments with artificial data.

Parameter	Value
Target space size	$3072 \times 3072 \times 1{,}600$ [nm]
Resolution of a low-resolution voxel	$192 \times 192 \times 400$ [nm]
Resolution of a high-resolution voxel	$24 \times 24 \times 50$ [nm]
Size of observed images	$16 \times 16 \times 4$
Number of molecules	3
Variance of Gaussian noise	$\sigma^2 = 9$
Rate parameter of Poisson noise	$\lambda = 4$

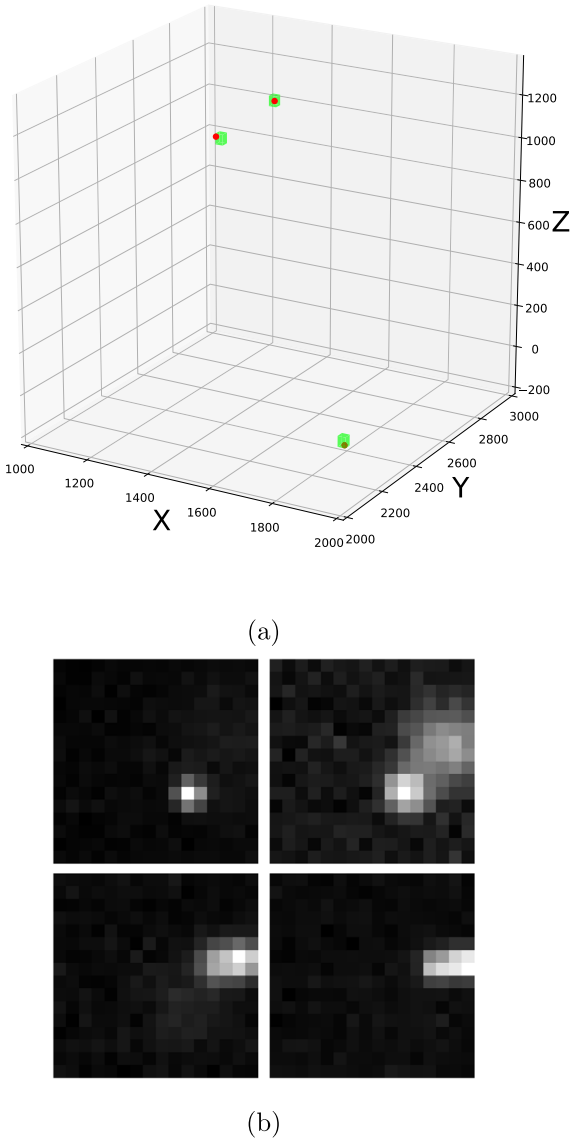

Fig. 6. (a) An example of artificial molecule distribution and a part of the target 3D space is shown for visualization purpose. True locations of molecules are shown by red circle and the voxels which contain the molecules are shown by green cuboid. (b) The observed image generated from the artificial distribution. Note that the images are normalized for visual emphasis.

whose molecule-existence probability exceeds a certain threshold. The thresholding value is common for all locations and needs to be specified by a user. Here, we selected 0.1 for the thresholding value. As demonstrated in Fig. 9(a), three molecules distributed in the 3D space are also accurately localized. Although, as Fig. 9 (b) indicates, the closely located molecules are difficult to localize, the estimated locations are close to the ground-truth locations. By plotting all the detected molecules from all frames, the helix curve structure behind the molecules can be observed in Fig. 9(c).

The processing speed of the network is presented in Fig. 10. As shown in the figure, the computational speed decreases as the size of the image increases and is inversely proportional to the number of pixels of an image. Because 22 images are obtained by our microscopy at every second, further improvement of the processing speed is required to process the large images in real-time. Still, the computational time is significantly reduced in comparison to the compressed sensing method. By solving the problem Eq. (9) by an alternating minimization, the processing speed is only 1.45×10^{-3} fps even for a small $16 \times 16 \times 4$ input.

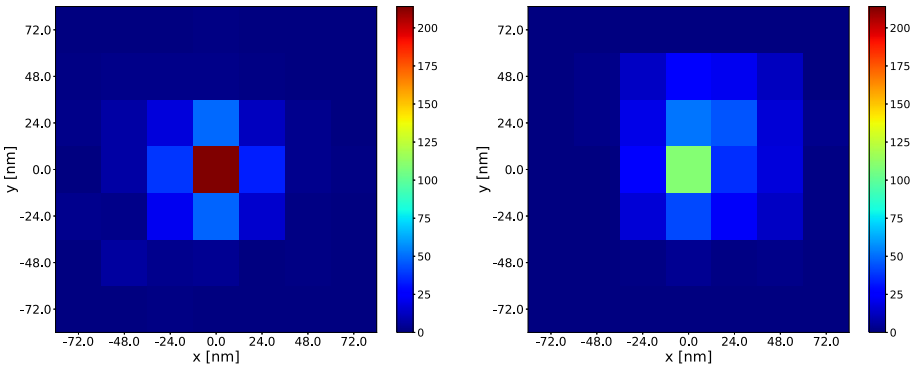

(a) Jaccard index=0.261 (b) Jaccard index=9.65×10^{-2}

Fig. 7. Histogram of the localization error of a single molecule. (a) the network that is trained to be robust against the lateral drift and (b) the network that is trained without considering the lateral drifts.

Table 3
Computational speed and accuracy of the CNN and compressed sensing method.

	CNN	Compressed sensing
Lateral error [nm]	16.7	57.6
Axial error [nm]	8.90	0.400
Frame per second	125	0.129

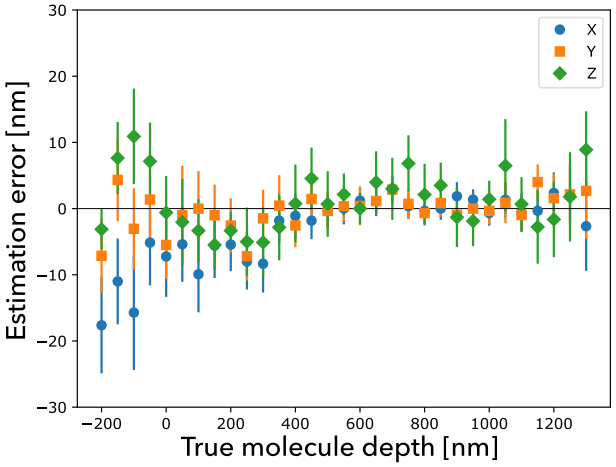

Fig. 8. Average estimation error along the horizontal (X), vertical (Y), and axial (Z) axes with their 95% confidence intervals.

4.3. Experiments with real images

In this section, we show the experimental results with real data that observed microtubules by our microscopy. In this experiment, there were no ground-truth results; hence, we used the trained neural network from the previous subsection to localized molecules.

The resolution of the low- and high-resolution images are the same as in the previous subsection. The size of the input images for each frame is $256 \times 256 \times 4$, and the target image size is $2048 \times 2048 \times 32$. An example of a frame is shown in Fig. 11. The dataset contains 39,000 frames of images, and each frame was processed independently to localize the molecules. In this experiment, we estimated that a molecule exists in a voxel if the molecule-existence probability exceeds 0.05.

Fig. 12 shows the estimated high-resolution image generated by merging localization results of all the frames. Each pixel of the image is a binary value, which indicates that the voxel contains a molecule in more than one frame. From the figures, we can observe a tubular structure of the microtubules, which varies depending on the depth.

5. Discussion

This study presents the 3D molecule localization problem using quad-plane microscopy. The problem with using MUM is lateral drift in the camera positions, which makes the localization less

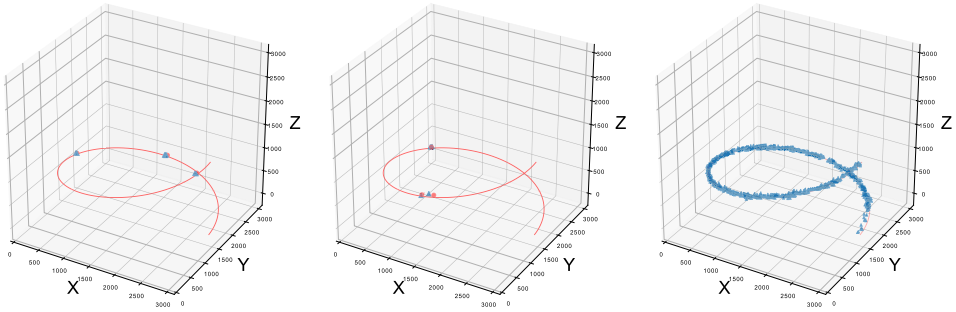

(a) Estimation result of $t = 6$ (b) Estimation result of $t = 43$ (c) Reconstructed image from 300 frames

Fig. 9. Localization results using artificial data. The red lines shows the true molecular structure from which molecules were sampled from. The red circles show true high-resolution molecule coordinates and the blue triangles show a estimated molecule locations. Figures (a) and (b) shows the estimation results of selected frames, and figure (c) shows the image reconstructed from 300 frames.

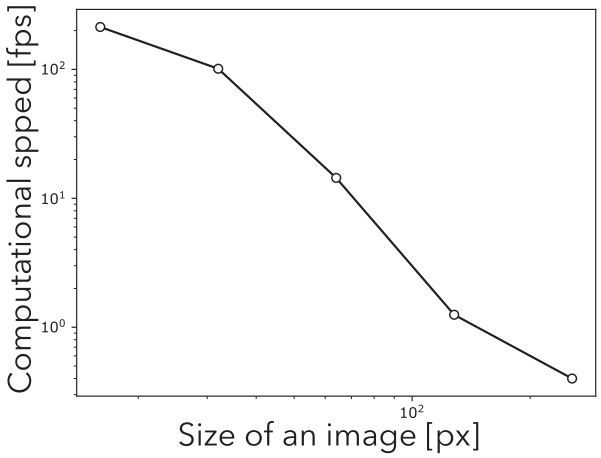

Fig. 10. Computational speed (fps) of estimations by the trained network for images of the size 16 px × 16 px, 32 px × 32px, . . . ,256 px × 256 px. The estimation speed of our network is inversely proportional to the number of pixels of an image.

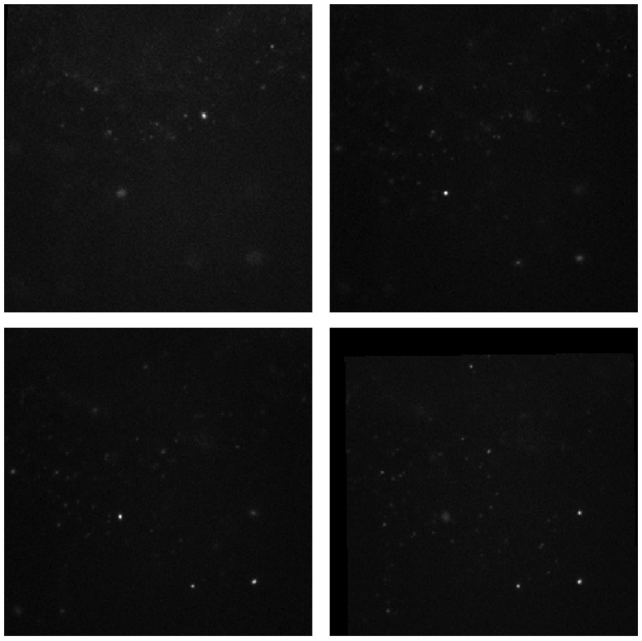

Fig. 11. A frame which observed and microtubules. The observed images is a 256 × 256 × 4 image and the difference in the field of view of the cameras was corrected by affine transformation.

accurate. We formulated the localization problem as a compressed sensing problem that consists of the molecule localization and an estimation of the amount of drifts. However, the computational cost to solve this problem is high, and the optimal solution cannot be obtained within a reasonable computational time. In this study, we used CNN to solve this problem accurately and efficiently. The network is trained to be robust against the sub-pixel-sized lateral drift in the camera locations. Therefore, the trained network can accurately estimate the locations of molecules in an observed image without explicitly estimating the amount of drift in the cameras.

Experiments with both artificial data and real data were presented. The results suggest that the network achieves 3D localization of the molecules with an average lateral resolution of 25 nm and an axial resolution of 50 nm. The trained network is also robust to the lateral drift in the camera positions and estimates

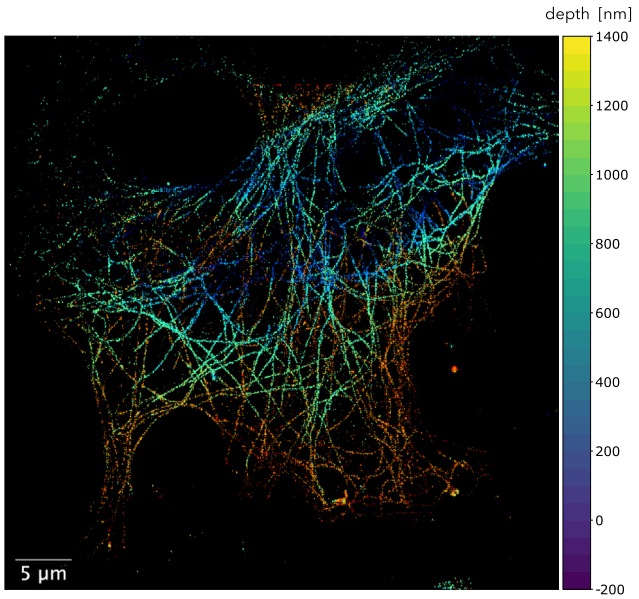

Fig. 12. Estimated high-resolution image of the microtubules data. The depth-dependent tubular structure of the sample is visualized by the colors.

the molecule location without estimating the amount of lateral drifts. We expect that this technique can be used to broaden the applicability of MUM to 3D imaging because an explicit drift correction is not required.

However, some limitations are worth noting. Although our proposed method significantly reduces the computational cost of solving the localization problem, large images are still difficult to process with real-time processing speed. Therefore, future work should include further improvement in computational speed. Using a faster method to extract possible molecule locations and localizing the molecule by the proposed method may further improve the computational efficiency.

CRediT authorship contribution statement

Toshimitsu Aritake: Conceptualization, Methodology, Software, Validation, Formal analysis, Writing - original draft, Visualization. **Hideitsu Hino:** Formal analysis, Conceptualization. **Shigeyuki Namiki:** Investigation. **Daisuke Asanuma:** Investigation. **Kenzo Hirose:** Supervision. **Noboru Murata:** Project administration.

Declaration of Competing Interest

The authors declare the following financial interests/personal relationships which may be considered as potential competing interests: Dr. Hideitsu Hino reports grants from Japan Society for the Promotion of Science KAKENHI Grant Numbers 17H01793 and grants from Japan Science and Technology Agency CREST Grant Number JPMJCR1761 during the conduct of the study.

Dr. Noboru Murata reports grants from Japan Society for the Promotion of Science KAKENHI Grant Numbers 17H01793 , 18H03291 and grants from Japan Science and Technology Agency CREST Grant.

Acknowledgments

The authors would like to thank M. Tanaka for technical assistance. This work was partially supported by JSPS KAKENHI (Grant Nos. 17H01793 and 18H03291) and JST CREST (Grant Nos. JPMJCR1761 and JPMJCR14D7).

References

[1] L. Schermelleh, A. Ferrand, T. Huser, C. Eggeling, M. Sauer, O. Biehlmaier, G.P. Drummen, Super-resolution microscopy demystified (jan 2019). doi:10.1038/s41556-018-0251-8.

[2] E. Betzig, G.H. Patterson, R. Sougrat, O.W. Lindwasser, S. Olenych, J.S. Bonifacino, M.W. Davidson, J. Lippincott-Schwartz, H.F. Hess, Imaging intracellular fluorescent proteins at nanometer resolution, Science 313 (5793) (2006) 1642–1645, https://doi.org/10.1126/science.1127344.

[3] S.T. Hess, T.P. Girirajan, M.D. Mason, Ultra-high resolution imaging by fluorescence photoactivation localization microscopy, Biophysical Journal 91 (11) (2006) 4258–4272, https://doi.org/10.1529/biophysj.106.091116.

[4] W. Liu, K.C. Toussaint, C. Okoro, D. Zhu, Y. Chen, C. Kuang, X. Liu, Breaking the axial diffraction limit: a guide to axial super-resolution fluorescence microscopy, Laser and Photonics Reviews 12 (8) (2018) 1–29, https://doi.org/10.1002/lpor.201700333.

[5] B. Huang, W. Wang, M. Bates, X. Zhuang, Three-dimensional super-resolution imaging by stochastic optical reconstruction microscopy, Science 319 (5864) (2008) 810–813, https://doi.org/10.1126/science.1153529.

[6] S.R.P. Pavani, M.A. Thompson, J.S. Biteen, S.J. Lord, N. Liu, R.J. Twieg, R. Piestun, W.E. Moerner, Three-dimensional, single-molecule fluorescence imaging beyond the diffraction limit by using a double-helix point spread function, Proceedings of the National Academy of Sciences 106 (9) (2009) 2995–2999, https://doi.org/10.1073/pnas.0900245106.

[7] Y. Shechtman, S.J. Sahl, A.S. Backer, W.E. Moerner, Optimal point spread function design for 3d imaging, Physical Review Letters 113 (2014) 133902, https://doi.org/10.1103/PhysRevLett.113.133902.

[8] S. Ram, P. Prabhat, J. Chao, E.S. Ward, R.J. Ober, High accuracy 3D quantum dot tracking with multifocal plane microscopy for the study of fast intracellular dynamics in live cells, Biophysical Journal 95 (12) (2008) 6025–6043, https://doi.org/10.1529/biophysj.108.140392.

[9] H.P. Babcock, Multiplane and spectrally-resolved single molecule localization microscopy with industrial grade CMOS cameras, Scientific Reports 8 (1) (2018) 1726, https://doi.org/10.1038/s41598-018-19981-z.

[10] M.J. Mlodzianoski, J.M. Schreiner, S.P. Callahan, K. Smolková, A. Dlasková, J. Šantorová, P. Ježek, J. Bewersdorf, Sample drift correction in 3d fluorescence photoactivation localization microscopy, Optics Express 19 (16) (2011) 15009–15019, https://doi.org/10.1364/OE.19.015009.

[11] Y. Wang, J. Schnitzbauer, Z. Hu, X. Li, Y. Cheng, Z.-L. Huang, B. Huang, Localization events-based sample drift correction for localization microscopy with redundant cross-correlation algorithm, Optics Express 22 (13) (2014) 15982–15991, https://doi.org/10.1364/OE.22.015982.

[12] D.L. Donoho, Compressed sensing, IEEE Transactions on Information Theory 52 (4) (2006) 1289–1306, https://doi.org/10.1109/TIT.2006.871582.

[13] A. Lucas, M. Iliadis, R. Molina, A.K. Katsaggelos, Using deep neural networks for inverse problems in imaging: Beyond analytical methods, IEEE Signal Processing Magazine 35 (1) (2018) 20–36, https://doi.org/10.1109/MSP.2017.2760358.

[14] K. Gregor, Y. LeCun, Learning fast approximations of sparse coding, in: Proceedings of the 27th International Conference on Machine Learning, ICML'10, Omnipress, Madison, WI, USA, 2010, p. 399–406.

[15] J.R. Hershey, J.L. Roux, F. Weninger, Deep unfolding: Model-based inspiration of novel deep architectures, ArXiv abs/1409.2574.

[16] P. Zelger, K. Kaser, B. Rossboth, L. Velas, G.J. Schütz, A. Jesacher, Three-dimensional localization microscopy using deep learning, Optics Express 26 (25) (2018) 33166–33179, https://doi.org/10.1364/OE.26.033166.

[17] W. Ouyang, A. Aristov, M. Lelek, X. Hao, C. Zimmer, Deep learning massively accelerates super-resolution localization microscopy, Nature Biotechnology 36 (5) (2018) 460–468, https://doi.org/10.1038/nbt.4106.

[18] E. Nehme, L.E. Weiss, T. Michaeli, Y. Shechtman, Deep-storm: super-resolution single-molecule microscopy by deep learning, Optica 5 (4) (2018) 458–464, https://doi.org/10.1364/OPTICA.5.000458.

[19] N. Boyd, E. Jonas, H. Babcock, B. Recht, Deeploco: Fast 3d localization microscopy using neural networks, bioRxivdoi:10.1101/267096.

[20] P. Zhang, S. Liu, A. Chaurasia, D. Ma, M.J. Mlodzianoski, E. Culurciello, F. Huang, Analyzing complex single-molecule emission patterns with deep learning, Nature Methods 15 (11) (2018) 913–916, https://doi.org/10.1038/s41592-018-0153-5.

[21] E. Hershko, L.E. Weiss, T. Michaeli, Y. Shechtman, Multicolor localization microscopy and point-spread-function engineering by deep learning, Optics Express 27 (5) (2019) 6158–6183, https://doi.org/10.1364/OE.27.006158.

[22] L. Möckl, A.R. Roy, P.N. Petrov, W.E. Moerner, Accurate and rapid background estimation in single-molecule localization microscopy using the deep neural network bgnet, Proceedings of the National Academy of Sciences 117 (1) (2020) 60–67, https://doi.org/10.1073/pnas.1916219117.

[23] C. Dong, C.C. Loy, X. Tang, Accelerating the super-resolution convolutional neural network, in: B. Leibe, J. Matas, N. Sebe, M. Welling (Eds.), Computer Vision – ECCV 2016, Springer International Publishing, Cham, 2016, pp. 391–407.

[24] T. Hastie, R. Tibshirani, M. Wainwright, Statistical Learning with Sparsity: The Lasso and Generalizations, Chapman & Hall/CRC, 2015.

[25] L. Gu, Y. Sheng, Y. Chen, H. Chang, Y. Zhang, P. Lv, W. Ji, T. Xu, High-density 3D single molecular analysis based on compressed sensing, Biophysical Journal 106 (11) (2014) 2443–2449, https://doi.org/10.1016/j.bpj.2014.04.021.

[26] S. Ioffe, C. Szegedy, Batch normalization: Accelerating deep network training by reducing internal covariate shift, in: Proceedings of the 32nd International Conference on Machine Learning - vol. 37, ICML'15, JMLR.org, 2015, pp. 448–456.

[27] D.W. Cleveland, K.F. Sullivan, Molecular biology and genetics of tubulin, Annual Review of Biochemistry 54 (1) (1985) 331–366, https://doi.org/10.1146/annurev.bi.54.070185.001555, pMID: 3896122.

[28] D.P. Kingma, J. Ba, Adam: A method for stochastic optimization, in: 3rd International Conference on Learning Representations, ICLR 2015, San Diego, CA, USA, May 7–9, 2015, Conference Track Proceedings, 2015.

Toshimitsu Aritake received the B.Eng. and M.Eng. from Waseda University in 2012 and 2014. He joined Hitachi's Central Research Laboratory and worked as a research staff from April 2014 to September 2017. Since October 2017, he has been working toward the Doctor's degree at Waseda University. His research interests include machine learning such as sparse modeling, matrix factorization and deep learning.

Hideitsu Hino received his bachelor's degree in engineering in 2003, and a master's degree in Applied Mathematics and Physics in 2005 from Kyoto University. He was with Hitachi's Systems Development Laboratory from April 2005 to August 2007. He earned D. Eng. in 2010 from Waseda University. From April 2013 to 2018, he was an Assistant and Associate Professor at University of Tsukuba, and he is currently a Professor at The Institute of Statistical Mathematics. His research interests include analysis of learning algorithms and the application of statistical methods to various problems.

Shigeyuki Namiki received the B.Sc. and M.Sc. from the University of Tsukuba and received a Ph.D. from the University of Tokyo in 2002. He was an assistant professor in 2007 in the Department of Cell Physiology at Nagoya University. He was an assistant professor in 2009 and is currently a lecturer in the Department of Neurobiology at the University of Tokyo. His research interest is the relationship between the dynamics of synaptic molecules and synaptic plasticity.

Daisuke Asanuma is an Assistant Professor in the Department of Pharmacology at the University of Tokyo since 2018. He is also a Japan Science and Technology Agency (JST)-PRESTO researcher since 2017. From 2011 to 2018, he served as an Assistant Professor in the Department of Neurobiology at the University of Tokyo. He received his Ph.D. in 2011 from the University of Tokyo. He was a Research Fellow of the Japan Society for the Promotion of Science (JSPS) from 2008 to 2011. He has been involved in development of chemical tools for biological and medical applications such as fluorescence imaging of bioactive molecules and in vivo tumor imaging.

Kenzo Hirose is a Professor in the Department of Pharmacology at the University of Tokyo since 2016. From 2008 to 2018 he served as a professor in the Department of Neurobiology. From 2005 to 2008 he served as a professor in the Department of Cell Physiology at Nagoya University. He earned his M.D. in 1992 and received his Ph.D. in 1996 in the University of Tokyo. He is interested in the cellular signaling and has been developing new technologies to visualize signaling molecules in living cells.

Noboru Murata received the B. Eng., M. Eng. and Dr. Eng. in Mathematical Engineering and Information Physics from the University of Tokyo in 1987, 1989 and 1992, respectively. After working at the University of Tokyo, GMD FIRST in Germany, and RIKEN in Japan, in April of 2000, he joined Waseda University in Japan where he is presently a professor. His research interest includes the theoretical aspects of learning machines such as neural networks, focusing on the dynamics and statistical properties of learning.